Visualizing bulk band structure in Fe_4N thin films by spin- and angle-resolved photoelectron spectroscopy

Karen Nakanishi,[1,*] Masaaki Kakoki,[1,*] Kiyotaka Ohwada,[1] Kenta Kuroda,[1,2,3] Kazuki Sumida,[4,5] Hitoshi Sato,[5] Koji Miyamoto,[5] Taichi Okuda,[2,3,5] Shinji Isogami,[6,†] Keisuke Masuda,[6,‡] Yuya Sakuraba,[6] and Akio Kimura[1,2,3,7,§]

[1]*Physics Program, Graduate School of Advanced Science and Engineering, Hiroshima University, 1-3-1 Kagamiyama, Higashi-Hiroshima 739-8526, Japan*

[2]*International Institute for Sustainability with Knotted Chiral Meta Matter (WPI-SKCM²), 1-3-1 Kagamiyama, Higashi-Hiroshima 739-8531, Japan*

[3]*Research Institute for Semiconductor Engineering, 1-4-2 Kagamiyama, Higashi-Hiroshima, Hiroshima 739-8527, Japan*

[4]*Materials Sciences Research Center, Japan Atomic Energy Agency, Hyogo 679-5148, Japan*

[5]*Research Institute for Synchrotron Radiation Science (HiSOR), Hiroshima University, 2-313 Kagamiyama, Higashi-Hiroshima 739-0046, Japan*

[6]*National Institute for Materials Science, 1-2-1 Sengen, Tsukuba 305-0047, Japan*

[7]*Synchrotron Radiation Research Center, National Institutes for Quantum Science and Technology (QST), Sayo, Hyogo, Japan*

(Received 18 May 2025; accepted 3 May 2026; published 8 June 2026)

The bulk band structure of an *in situ* prepared ferromagnetic Fe_4N thin film has been investigated using spin- and angle-resolved photoelectron spectroscopy with synchrotron radiation. It was observed that most of the bands near the Fermi level are of minority spin. The experimental results are well reproduced by first-principles calculations. Our orbital analysis of the band structure has revealed that the electron pocket near the Γ point is primarily attributed to the Fe $3d_{xy}$ orbital of the Fe(II) site, while the electron pocket near the M point is associated with the Fe(II) $3d_{z^2}$ orbital. Our observation of real band structure in Fe_4N thin films could provide valuable insight into the properties of anisotropic magnetoresistance and anomalous Nernst effect.

DOI: 10.1103/mlcy-gszb

I. INTRODUCTION

Utilizing the spin degree of freedom of electrons in materials has been a key approach to realizing highly efficient spintronic devices. For instance, magnetic random-access memories and read heads of hard disk drives nowadays incorporate magnetic tunnel junctions (MTJs) [1,2], which exhibit high (low) electrical resistance at the antiparallel (parallel) magnetic configurations of two ferromagnetic layers. The tunneling magnetoresistance (TMR) ratio, i.e., the resistance change in such two configurations, is determined by the spin polarization of the density of states at the Fermi level (P_{DOS}). Consequently, numerous studies have been conducted to develop ferromagnetic materials with a substantial P_{DOS}.

However, the recent trend is moving toward more advanced functionalities, driving the development of spintronic devices such as logic-in memories [3] and spin-torque nano-oscillators [4]. Under these circumstances, various approaches are being explored to realize these devices, going beyond the existing concept of high P_{DOS}. An encouraging approach to address this issue is the implementation of antiperovskite transition metal nitride systems [5]. These materials possess a perovskite crystal structure denoted as ANB_3, where A and B represent various $3d$ transition metals, such as Mn, Fe, and Co. The preferential sites of A and B correspond to the corner and face center of the unit cells, respectively, while N is ordered at the octahedral center in the sublattice of B as an interstitial impurity, due to its smaller atomic radius compared to atoms A and B. A variety of tunable physical properties has been reported in many systems with ANB_3 so far [5–8]. Among these systems, Fe_4N ($A = B =$ Fe) [Fig. 1(b)] displays ferromagnetism with a Curie temperature of 760 K and various spin-transport properties attributed to its perfect spin polarization with a negative sign, as predicted by Kokado *et al.* [9]. Epitaxial thin films of Fe_4N can be grown via molecular-beam epitaxy [10–12] and sputtering techniques [13–20], making it a material of considerable interest for magnetic and spintronic applications. In particular, the inverse properties, where high (low) electrical resistance is observed for parallel (antiparallel) magnetization configurations between the magnetic free and pinned layers, have been demonstrated in MTJs with Fe_4N electrodes [21]. This phenomenon is referred to as the inverse-TMR effect, which has been drastically enhanced by using the Cu underlayer on the Si substrate [22]. Such an enhanced inverse-TMR ratio could lead to a practical device based on the phenomenon of inverse current-induced magnetization switching

*These authors contributed equally to this work.
†Contact author: isogami.shinji@nims.go.jp
‡Contact author: masuda.keisuke@nims.go.jp
§Contact author: akiok@hiroshima-u.ac.jp

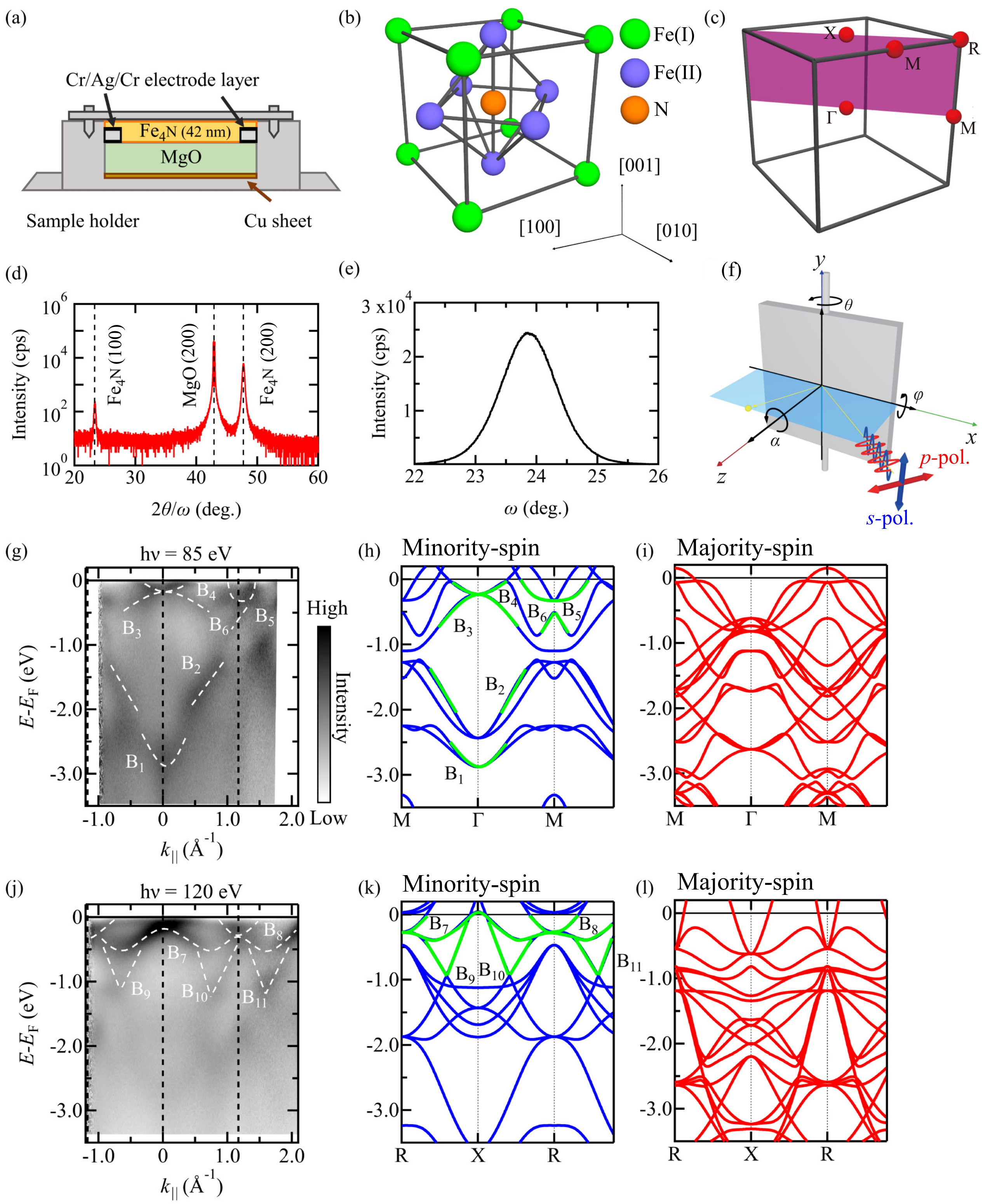

FIG. 1. (a) Geometry of Fe_4N thin film on MgO substrate with sample holder for ARPES experiment. (b) Crystal structure and (c) Brillouin zone of Fe_4N. (d) Out-of-plane x-ray diffraction profiles and (d) rocking curve of Fe_4N thin film. (f) ARPES measurement geometry. Here, θ, φ, and α denote polar, tilt, and azimuthal angles, respectively. ARPES E-$k_{\parallel}$ frame of Fe_4N thin film acquired at $h\nu = 85$ eV [panel (g)] and 120 eV [panel (j)]. Calculated minority- [majority-] spin band structure along (h) [(i)] M-Γ-M and (k) [(l)] R-X-R lines. The calculated band structures are rigidly shifted downward by 0.2 eV to account for hole doping.

[23]. Furthermore, Fe_4N thin films have exhibited a variety of unusual and intriguing device-related properties, such as inverse current-perpendicular-to-plane giant magnetoresistance (CPP-GMR) [24], large negative anisotropic magnetoresistance (AMR) with a characteristic fourfold symmetry [25], and a sizable anomalous Nernst effect (ANE) [26,27]. In addition, the anomalous Hall effect in Fe_4N shows a strong temperature dependence, further highlighting the unique and complex transport behavior of this material [28]. Various characteristic transport and thermoelectric phenomena observed in Fe_4N are believed to be associated with its minority-spin-dominated electronic band structure; however, spin-resolved electronic bands have not yet been experimentally observed. In this respect, it is crucial to experimentally elucidate the band dispersions and their symmetries of Fe_4N, as this would facilitate a better understanding of electron transport phenomena and open up opportunities for the development of materials with enhanced functionality.

Angle-resolved photoelectron spectroscopy (ARPES) is a powerful experimental technique that enables the visualization of the band structure of materials. However, when employing conventional light sources in the vacuum ultraviolet region, ARPES exhibits high surface sensitivity due to the short mean free path of photoelectrons. As a consequence, this experimental method is typically applied to materials with cleavage planes, such as layered superconductors and transition metal chalcogenides [29]. On the other hand, for nonlayered materials, ARPES has been restricted to elemental crystals for which surface-cleaning procedures have been established. The surface cleaning of multielement compounds presents challenges since sputtering and annealing procedures have element-dependent sputtering rates, which can alter surface stoichiometry. Therefore, the ARPES on bulk crystals of Fe_4N remains a challenge due to the lack of an established surface-cleaning procedure. To address this issue, we employed thin-film samples of Fe_4N grown on MgO substrates and loaded them into the ARPES experimental setup without breaking the vacuum, utilizing an ultrahigh-vacuum suitcase. In this article, we successfully observed bulk-driven band dispersions using ARPES with synchrotron radiation. Spin-resolved measurements revealed that most of the observed bands are of minority spin. The experimental results are reasonably well reproduced by first-principles calculations. Our findings may provide insights into the characteristic transport and thermoelectric phenomena observed in Fe_4N.

II. EXPERIMENTAL

Using a reactive magnetron nitride sputtering technique, a 42-nm-thick γ'-Fe_4N epitaxial film was deposited on a MgO(001) substrate at a substrate temperature of 450 °C at the National Institute of Materials Science. Electrodes consisting of Cr/Ag/Cr thick multilayers were formed between the MgO substrate and the Fe_4N film for the ground connection, as shown in Fig. 1(a). The possible crystal structure is depicted in Fig. 1(b), indicating an antiperovskite structure with three sublattices: the corner Fe [Fe(I)], face-center Fe [Fe(II)], and body-center N [30]. The structural analysis was performed by x-ray diffraction (XRD).

ARPES and spin-ARPES measurements were conducted using synchrotron radiation at incident photon energies of 80–120 and 50–119 eV, respectively, at BL-7 and BL-9B of Research Institute for Synchrotron Radiation Science. The analysis of the photoelectron spin polarization was performed using a very-low-energy electron diffraction (VLEED)-type spin detector, with an effective Sherman function of 0.3, which was determined by a standard Bi thin film prior to the measurement [31–33]. After transportation from the vacuum suitcase, thin-film samples were postannealed at 400 °C for 30–60 min in an ultrahigh vacuum. The maintenance of stoichiometry in the samples was confirmed by Auger electron spectroscopy, and clean and well-ordered surfaces were validated by clear 1×1 low-energy electron diffraction (LEED) spots. The photoelectron spin polarization (P) was estimated from the measured intensity asymmetry $A = (I^+ - I^-)/(I^+ + I^-)$ with the effective Sherman function (S_{eff}) through the relation $P = A/S_{\mathrm{eff}}$, where I^+ (I^-) represents the reflected electron intensity at the positively (negatively) magnetized Fe target of the spin detector. See the Supplemental Material [34] for further details of the experimental procedures, surface characterization, and computational methods.

III. RESULTS AND DISCUSSION

Figure 1(d) shows the out-of-plane XRD profile for the Fe_4N film. Two diffraction peaks were observed at $2\theta/\omega \approx 23.4^\circ$ and 47.8°, which originate from the $Fe_4N(100)$ superlattice and $Fe_4N(200)$ fundamental lattice, respectively. The XRD intensity for both peaks was evaluated by fitting with the pseudo-Voigt function, following the same procedure as in our previous study [35]. The degree of order of Fe and N was estimated to be 0.78, suggesting an agreement with previous studies. Figure 1(e) shows the rocking curve for the (200) plane. The full width at half maximum was evaluated to be 1.1°, indicating that the deviation of the crystal orientation along the perpendicular direction to the film plane was small [36].

Electronic energy dispersions were experimentally obtained along the [110] direction in the incident photon energy ($h\nu$) range of 80–120 eV with a 5 eV increment between each step. It corresponds to the energy dispersions on the ΓMRX plane of the Brillouin zone [Fig. 1(c)], where the ARPES geometry is shown in Fig. 1(f). In Figs. 1(g) and 1(j), selected energy ARPES images in the E-$k_\parallel$ frame acquired at $h\nu = 85$ and 120 eV are presented. The images demonstrate a parabolic energy dispersion that exhibits an energy minimum near the zone center ($k_\parallel = 0$ Å^{-1}) and measures approximately -2.8 eV from the Fermi level (E_F) (feature B_1). One can see a pair of steep energy dispersions spanning the energy range from -2.0 to -1.3 eV (B_2). In the vicinity of the E_F and $k_\parallel = 0$ Å^{-1} of the image at $h\nu = 85$ eV, there are two parabolic dispersions, one downward (B_3) and the other upward (B_4), which touch at -0.2 eV and $k_\parallel = 0$ Å^{-1}. Additionally, at $k_\parallel = 1.2$ Å^{-1}, a small electron pocket (B_5) and a steep dispersion intersecting the E_F (B_6) are observed near the zone boundary. At $h\nu = 120$ eV, a different feature is noticeable, as the upward dispersion observed at 85 eV diminishes, while the downward dispersion is still visible (B_7), exhibiting an oscillation as depicted in Fig. 1(j). A small electron pocket labeled B_8 is seen at the zone boundary ($k_\parallel = 1.2$ Å^{-1}). By

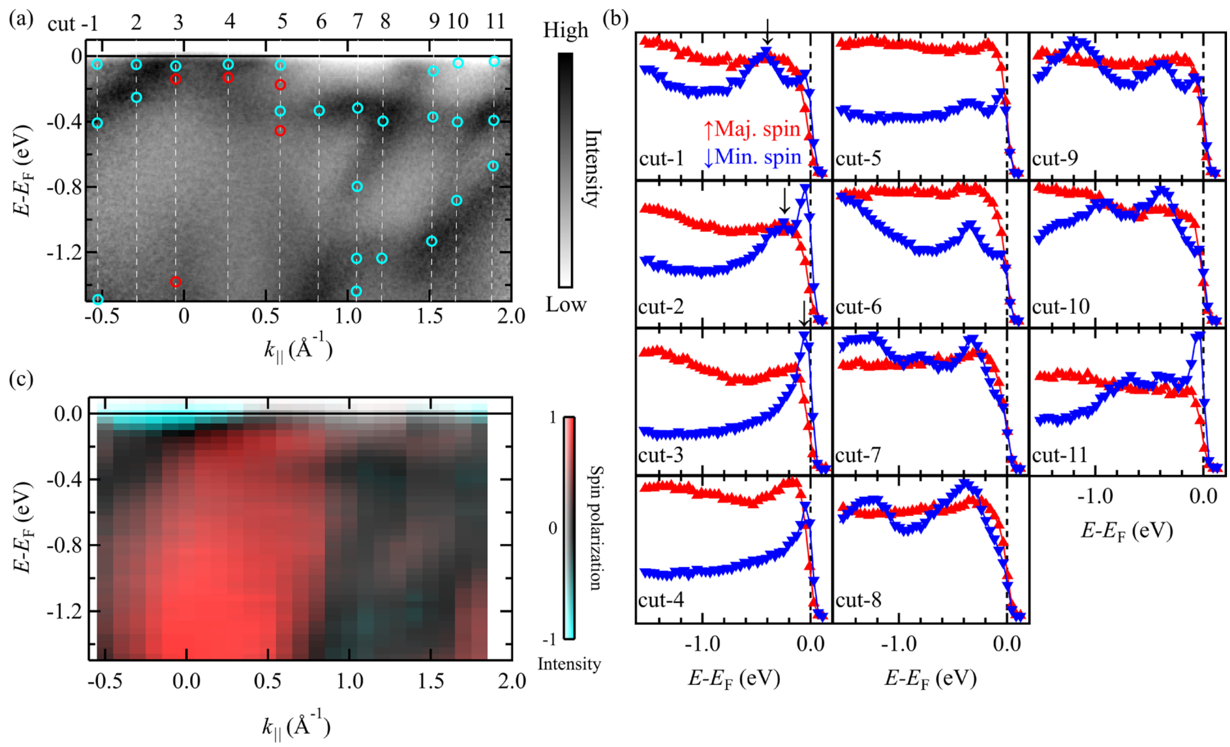

FIG. 2. (a) ARPES snapshot and (c) its spin polarization map in E-$k_{\parallel}$ frame of Fe_4N thin film acquired at $h\nu = 85$ eV. (b) Spin-resolved energy distribution curves in majority-spin (red) and minority-spin (blue) channels along several $k_{\parallel}$ cuts (numbered 1–11) displayed in panel (a).

comparing the experimentally observed ARPES energy dispersions with the calculated band structures [Figs. 1(h), 1(i), 1(k), and 1(l)], we find that the experimentally observed pair of downward and upward energy dispersions at $h\nu = 85$ eV [B_3 and B_4 in Fig. 1(g)] is well reproduced in the calculation for the minoriy-spin channel along the M-Γ-M line as shown with thick green curves in Fig. 1(h). The calculation also shows two electron pockets crossing E_F near the M point, with one that corresponds to the observed ARPES result at $h\nu = 85$ eV [B_5 in Fig. 1(h)]. The calculated energy dispersions in the minority-spin channel along the R-X-R line [Fig. 1(k)] also show only downward dispersions around the X point, consistent with the experimental result at $h\nu = 120$ eV. The good correspondence between experiment and theory allows us to conclude that the ARPES results taken at $h\nu = 85$ and 120 eV trace the electronic states at $k_z = 0$ and π/a (a is the lattice constant of Fe_4N), respectively. It should be noted here that none of the calculated majority-spin dispersions in Figs. 1(i) and 1(l) match with the experimentally observed band dispersions in Figs. 1(g) and 1(j). It is noted that some of the calculated bands are not clearly observed in the experimental spectra, which can be attributed to photoemission matrix-element effects, k_z broadening, and spin-dependent spectral-weight redistribution. Similar situations have been discussed in previous ARPES studies of magnetic and correlated materials, where the overall topology of the electronic structure can still be reliably interpreted even when some calculated bands are not clearly observed in the experimental spectra [37–40]. Nevertheless, the overall topology and connectivity of the minority-spin bands are well reproduced by the calculations. The majority-spin spectra appear to be substantially broadened due to the shorter lifetime of majority-spin holes compared to their minority-spin counterparts [41], making experimental identification difficult.

To further confirm the spin characteristics of the observed ARPES energy dispersions in Figs. 1(g) and 1(j) by experiments, we conducted the spin-ARPES measurements. Figures 2(a) and 2(b) display the ARPES image at 85 eV and the spin-resolved energy distribution curves (EDCs) along several $k_{\parallel}$ cuts (1–11) denoted with dashed lines in Fig. 2(a). On the ARPES image in Fig. 2(a), the local intensity maxima of the majority- and minority-spin EDCs are indicated by red and light blue open circles, respectively. It is noticed from cut 1 ($k_{\parallel} = -0.5$ Å^{-1}) in Fig. 2(b) that two peak structures are present at $E - E_F = 0$ and -0.4 eV in the minority-spin channel, whereas the majority-spin EDC is relatively featureless. The peak at -0.4 eV in the minority-spin channel approaches toward E_F as the cut moves from 1 ($k_{\parallel} = -0.5$ Å^{-1}) to 2 ($k_{\parallel} = -0.2$ Å^{-1}) and ultimately merges with the peak at E_F in cut 3 ($k_{\parallel} = 0$ Å^{-1}) as indicated by the arrows. The intensity of the minority-spin peak at E_F increases from cut 1 to cut 3. These results indicate that the observed downward and upward parabolic dispersions that touch at the zone center [B_3 and B_4 in Fig. 1(h)] have minority-spin characteristics. It is also found that the flat band (B_5) and the steeply dispersing band (B_6) near the zone boundary ($k_{\parallel} = 1.2$ Å^{-1}) exhibit minority-spin character, as evidenced by the corresponding plots in Fig. 2(a). A spin-polarization image in the ARPES E-$k_{\parallel}$ frame is shown in Fig. 2(c), where positive spin polarization is observed in a wide range of the frame. The predominance of positive spin polarization is mainly due to the positively spin-polarized

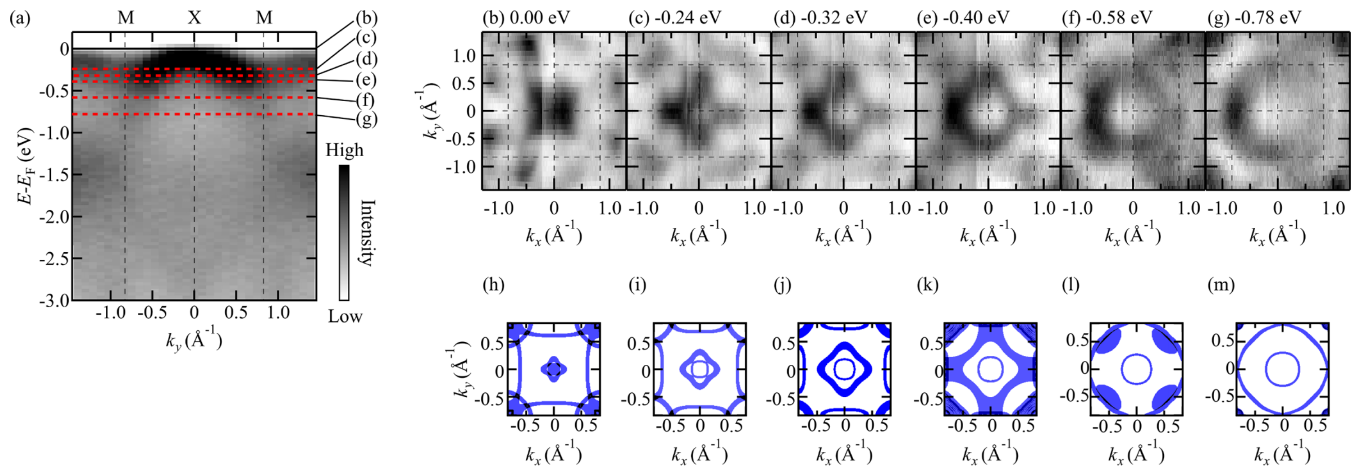

FIG. 3. (a) ARPES E-$k_\parallel$ dispersions taken at $h\nu = 118$ eV in the [010] (M-X-M) line. (b)–(g) Experimental and (h)–(m) calculated constant energy surfaces from $E - E_F = 0$ to -0.78 eV.

secondary electron background typically observed in ferromagnets [42]. The featureless majority-spin spectra are again consistent with the shorter hole lifetime in the majority-spin channel compared to that in the minority-spin counterpart. On the other hand, negative spin polarization dominates in the vicinity of E_F, which is consistent with the spin-polarized EDCs, where most of the observed ARPES energy dispersions are assigned to the minority-spin bands.

Moving on to the experimental E-$k_\parallel$ dispersion taken at $h\nu = 118$ eV along the [010] (M-X-M) line, as shown in Fig. 3(a), we observe W-shaped energy dispersion that reaches an energy minimum (maximum) at the M (X) point. Figures 3(b)–3(g) display the constant energy slices. At $E - E_F = 0$ eV, a square-shaped pattern is observed in the center. At $E - E_F = -0.24$ and -0.32 eV, we find a diamond-shaped pattern surrounding the central X point, as well as a fourfold symmetric pattern with some intensity near the four corner R points. As the energy decreases, the central diamond-shaped pattern increases in size and evolves into a circular-shaped pattern, as seen in Figs. 3(f) and 3(g). These features are reasonably reproduced with the minority-spin part of the calculated constant energy contour as shown in Figs. 3(h)–3(m).

Henceforth, we gain a better understanding of the orbital properties of each energy dispersion that intersects E_F, which likely contributes to various electron conductivity phenomena. A depiction of Fe 3d orbital-specific energy dispersions in the minority-spin channel is shown in Fig. 4. Fe 3d electrons have a photoionization cross section approximately 35 times greater than that of N 2p electrons and 83 times larger than that of Fe 4p electrons at $h\nu = 100$ eV [43]. As a result, the observed ARPES energy dispersions stem mostly from Fe 3d orbitals. To deduce orbital components for ARPES energy dispersions along the M-X-M line, we consider the dipole selection rule for the p polarization of the incident photon. The feasible options for observable Fe 3d orbitals can be narrowed down to three ($d_{x^2-y^2}$, d_{z^2}, and d_{zx} orbitals), all of which have even parity with respect to the xz mirror coinciding with the measurement plane spanned by photon propagation and photoelectron emission vectors as schematically shown in the upper part of Fig. 4(c). The W-shaped energy dispersion near E_F along the M-X-M line observed in Fig. 3(a) is now interpreted to be mostly composed of the $d_{x^2-y^2}$ orbital (e_g) as shown in Fig. 4(a). Along the M-Γ-M line, the observable Fe 3d orbitals are d_{z^2} and d_{xy} as schematically depicted in the lower part of Fig. 4(c). By comparing the theoretical results shown in Fig. 4(b) with the experimental data in Fig. 1(g), it becomes clear that the deeper-lying states, such as B_1 and B_2, can be readily assigned to the d_{z^2} and d_{xy} orbitals, respectively. The characteristic pair of downward and upward parabolic bands close to the Γ point, which correspond to the features B_3 and B_4 in the ARPES image at $h\nu = 85$ eV in Fig. 1(h), is thought to be mostly composed of the d_{xy} orbital, while the electron pockets at the M point (B_5) with a flat bottom are contributed by the d_{z^2} orbital [see Fig. 4(b)]. See the Supplemental Material [34] for additional orbital-resolved band-structure analysis.

The spin polarization of conduction electron is predicted to be $P_\sigma = \frac{\sigma^\uparrow - \sigma^\downarrow}{\sigma^\uparrow + \sigma^\downarrow} = -1.0$, where $\sigma^{\uparrow(\downarrow)}$ represents the conductivity of the majority- (minority-) spin channel. Notably, the component of 3d minority spin dominates the entire conductivity, which is a specific characteristic of Fe_4N [9]. Since all the observed bands intersecting E_F are of minority-spin origin as exemplified by the EDCs for cut 2 and/or cut 3 [Fig. 3(b)], the perfectly spin-polarized nature of conduction electrons is strongly supported. Additionally, most of the observed ARPES energy dispersions primarily originate from the 3d orbitals of Fe, as inferred from the dispersion in Fig. 4. This can be understood through the present spin-resolved ARPES results, compared with first-principles calculations.

Hence, we conclude that the predicted 3d minority-spin conduction in Fe_4N can be supported by the results of ARPES in this study. A spin polarization value of $P_\sigma = -1.0$ holds the promise of enhanced and inverse output in the CPP-GMR spin valves. The inverse CPP-GMR effect was thus demonstrated in the Fe_4N/Ag/Fe spin valves by Li *et al.*, which can be attributed to the combined effects of negative P_σ in Fe_4N and positive P_σ in Fe [24]. Nonetheless, the magnitude of the CPP-GMR ratio does not fully reflect the potential of $P_\sigma = -1.0$. According to the CPP-GMR origin [44], not only the spin-asymmetry coefficient at a bulk β (related to P_σ) but also that at an interface γ play a role in boosting the magnitude of CPP-GMR ratio. Considering the electron flow from the

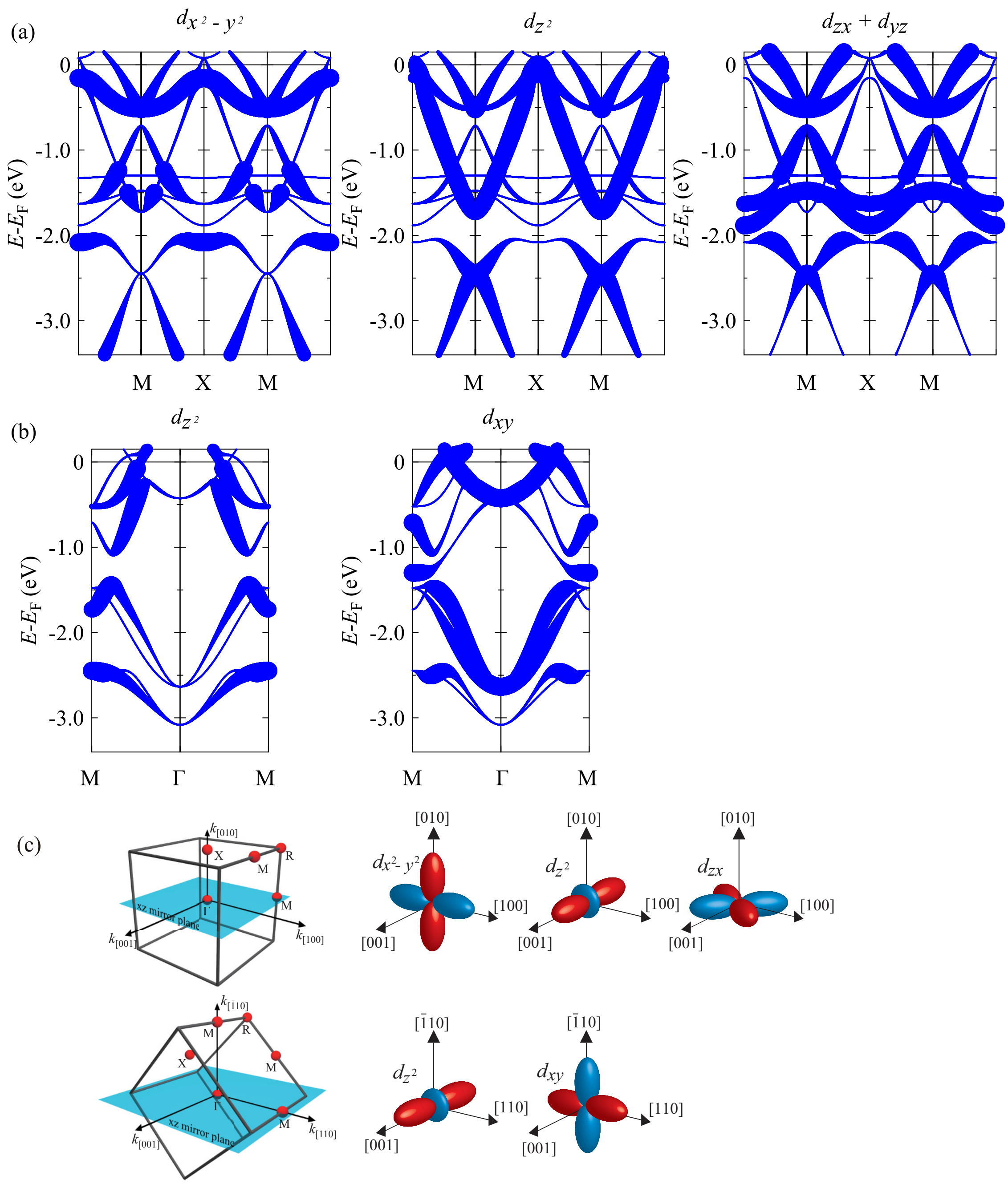

FIG. 4. Orbital components along (a) the M-X-M line and (b) the M-Γ-M line derived from first-principles calculations. The marker size corresponds to the weight of the orbitals, with their symmetries indicated above each panel. (c) Schematics of mirror planes (left) and electron orbitals with different symmetries (right). The calculated band structures are shown without energy shifting.

Fe_4N layer to the Fe layer in the Fe_4N/Ag/Fe spin valve, for example, 3d minority spin flips at the interface between Fe_4N and Ag spacer because of the less d-band state at the E_F of Ag, resulting in the suppression of γ. Consequently, the overall CPP-GMR ratio is suppressed no matter how large β in the Fe_4N.

Second, concerning the anisotropic ANE in the Fe_4N thin film, the in-plane ANE voltage along the [110] direction was observed to be larger than that along the [100] direction [26]. Upon examining the constant energy surfaces at $E_F =$ 0 to $-$ 0.4 eV [Fig. 3(b)], a distinctive diamond-shaped pattern is noticeable around the X point, coupled with a fourfold symmetrical pattern showing some intensity near the four R points. This offers one possible qualitative explanation for the in-plane anisotropic ANE. On the other hand, the diamond-shaped pattern near the E_F evolves into a circular shape at -0.58 and -0.78 eV [Figs. 3(f) and 3(g)], indicating the potential for controlling anisotropy in transport phenomena. We thus infer that the in-plane anisotropic ANE could be efficiently changed by tunning of E_F through the electron/hole doping and/or crystal strains.

Finally, we attempt to clarify a relation between the aforementioned orbital analysis and the observed negative-AMR effects in Fe_4N. The negative-AMR ratio of Fe_4N thin film exhibits a pronounced enhancement at temperatures below ∼50 K, coinciding with the emergence of a fourfold symmetric component ($C_{4\theta}$) in the in-plane field-angular dependence [25]. According to the extended two-current model, which incorporates *s*-*d* scattering [45], the origin of $C_{4\theta}$ can be elucidated through the splitting of 3*d* orbitals into five different orbitals, denoted as (d_{z^2}, $d_{x^2-y^2}$) and (d_{xy}, d_{yz}, d_{xz}), brought about by the discernible crystal field effect at low temperatures. Our orbital analysis, as presented in Fig. 4, uncovers contributions from both the d_{xz} and the d_{z^2} and $d_{x^2-y^2}$ to the bands intersecting the E_F. Therefore, we can confirm that the drastic enhancement in the negative-AMR ratio of Fe_4N is linked to these orbitals. To gain a more in-depth understanding of this phenomenon, a scattering analysis based on the Fermi surface would be necessary.

IV. CONCLUSION

To summarize, we employed the ARPES technique to investigate the band structure of Fe_4N thin films on MgO substrates using an ultra-high vacuum suitcase. Our observations revealed distinct energy dispersions along the M-Γ-M line, encompassing both upward and downward energy dispersions converging at the Γ point, as well as electron pockets near the M point. Spin-resolved analysis indicated that most of the bands intersecting E_F consist of minority spins, which accounts for the inverse TMR and negative AMR. The in-depth orbital analysis of the band structure demonstrates that the pair of parabolic bands near the Γ point is primarily composed of d_{xy} orbitals, while the electron pocket with a flat bottom near the M point is mainly comprised of d_{z^2} orbitals. These findings may also provide valuable insights into anisotropic properties observed in phenomena such as anisotropic magnetoresistance and the anisotropic anomalous Nernst effect.

ACKNOWLEDGMENTS

This work was financially supported by JSPS KAKENHI (Grants No. 17H06152, No. 20H00347, No. 24H01670, No. 24K21533, No. 24KK0107, No. 25H00743, and No. 25K01666), the JST FOREST Program (Grant No. JPMJFR236H), and the Yamada Science Foundation. The experiment was carried out at BL-7 and BL-9B of the Research Institute for Synchrotron Radiation Science (HiSOR) under Proposals No. 21BG045, No. 22AG041, and 22BG031.

DATA AVAILABILITY

The data that support the findings of this article are not publicly available. The data are available from the authors upon reasonable request.

[1] T. Miyazaki and N. Tezuka, Giant magnetic tunneling effect in Fe/Al_2O_3/Fe junction, J. Magn. Magn. Mater. **139**, L231 (1995).

[2] J. S. Moodera, L. R. Kinder, T. M. Wong, and R. Meservey, Large magnetoresistance at room temperature in ferromagnetic thin film tunnel junctions, Phys. Rev. Lett. **74**, 3273 (1995).

[3] S. Matsunaga, J. Hayakawa, S. Ikeda, K. Miura, H. Hasegawa, T. Endoh, H. Ohno, and T. Hanyu, Fabrication of a nonvolatile full adder based on logic-in-memory architecture using magnetic tunnel junctions, Appl. Phys. Express **1**, 091301 (2008).

[4] S. I. Kiselev, J. C. Sankey, I. N. Krivorotov, N. C. Emley, R. J. Schoelkopf, R. A. Buhrman, and D. C. Ralph, Microwave oscillations of a nanomagnet driven by a spin-polarized current, Nature (London) **425**, 380 (2003).

[5] S. Isogami and Y. K. Takahashi, Antiperovskite magnetic materials with 2*p* light elements for future practical applications, Adv. Electron. Mater. **9**, 2200515 (2023).

[6] J. M. D. Coey, D. Givord, and D. Fruchart, Metallic nitride and carbide perovskites: History and prospects, ECS J. Solid State Sci. Technol. **11**, 055002 (2022).

[7] Z. Zhang and W. Mi, Progress in ferrimagnetic Mn_4N films and its heterostructures for spintronics applications, J. Phys. D: Appl. Phys. **55**, 013001 (2022).

[8] K. Ito, S. Honda, and T. Suemasu, Transition metal nitrides and their mixed crystals for spintronics, Nanotechnology **33**, 062001 (2022).

[9] S. Kokado, N. Fujima, K. Harigaya, H. Shimizu, and A. Sakuma, Theoretical analysis of highly spin-polarized transport in the iron nitride Fe_4N, Phys. Rev. B **73**, 172410 (2006).

[10] J. L. Costa-Krämer, D. M. Borsa, J. M. García-Martín, M. S. Martín-González, D. O. Boerma, and F. Briones, Structure and magnetism of single-phase epitaxial γ'-Fe_4N, Phys. Rev. B **69**, 144402 (2004).

[11] M. Kimura and S. Hasegawa, Growth evolution of γ'-Fe_4N films on GaN(0001) and their interfacial structure, Jpn. J. Appl. Phys. **55**, 05FD02 (2016).

[12] H. Chatbi, M. Vergnat, P. Bauer, and G. Marchal, Growth and characterization studies of Fe_4N thin films prepared by ion beam assisted evaporation, Appl. Phys. Lett. **67**, 430 (1995).

[13] K. R. Nikolaev, I. N. Krivorotov, E. D. Dahlberg, V. A. Vas'ko, S. Urazhdin, R. Loloee, and W. P. J. Pratt, Structural and magnetic properties of triode-sputtered epitaxial γ'-Fe_4N films deposited on $SrTiO_3$ (001) substrates, Appl. Phys. Lett. **82**, 4534 (2003).

[14] L. L. Wang, X. Wang, W. T. Zheng, N. Ma, Q. F. Guan, J. Zhao, Y. Chen, and S. H. Feng, Synthesis of single nanocrystal phase γ'-Fe_4N on NaCl substrate by DC magnetron sputtering, Mater. Chem. Phys. **100**, 304 (2006).

[15] T. Ohgai, R. Shimono, H. Saitoh, and Y. Hayashi, Structure and soft magnetic properties of Fe–N thin films RF-sputtered on heated substrate, Mater. Trans. JIM **38**, 503 (1997).

[16] L. L. Wang, W. T. Zheng, J. Gong, H. B. Li, X. Wang, N. Ma, P. J. Cao, and X. C. Ma, Investigation on the structure and magnetic properties at low temperature for nanocrystalline γ'-Fe_4N thin films, J. Alloys Compd. **467**, 1 (2009).

[17] Y. Na, C. Wang, J. Xiang, N. Ji, and J. Wang, Investigation of γ'-Fe_4N thin films deposited on Si(100) and GaAs(100) substrates by facing target magnetron sputtering, J. Cryst. Growth **426**, 117 (2015).

[18] N. Pandey, S. Pütter, S. M. Amir, V. R. Reddy, D. M. Phase, J. Stahn, A. Gupta, and M. Gupta, Effect of interfacial in-

terdiffusion on magnetism in epitaxial Fe_4N films on $LaAlO_3$ substrates, Phys. Rev. Mater. **3**, 114414 (2019).

[19] S. Nagakura, Electronic structure of iron nitrides studied by electron diffraction. I. γ'-Fe_4N, J. Phys. Soc. Jpn. **25**, 488 (1968).

[20] S. Matar, P. Mohn, G. Demazeau, and B. Siberchicot, The calculated electronic and magnetic structures of Fe_4N and Mn_4N, J. Phys. France **49**, 1761 (1988).

[21] K. Sunaga, M. Tsunoda, K. Komagaki, Y. Uehara, and M. Takahashi, Inverse tunnel magnetoresistance in magnetic tunnel junctions with an Fe_4N electrode, J. Appl. Phys. **102**, 013917 (2007).

[22] Y. Komasaki, M. Tsunoda, S. Isogami, and M. Takahashi, 75% inverse magnetoresistance at room temperature in Fe_4N/MgO/CoFeB magnetic tunnel junctions fabricated on Cu underlayer, J. Appl. Phys. **105**, 07C928 (2009).

[23] S. Isogami, M. Tsunoda, Y. Komasaki, A. Sakuma, and M. Takahasi, Inverse current-induced magnetization switching in magnetic tunnel junctions with Fe_4N free layer, Appl. Phys. Express **3**, 103002 (2010).

[24] X. Li, H. Li, M. Jamali, and J.-P. Wang, Damping constant measurement and inverse giant magnetoresistance in spintronic devices with Fe_4N, AIP Adv. **7**, 125303 (2017).

[25] M. Tsunoda, H. Takahashi, S. Kokado, Y. Komasaki, A. Sakuma, and M. Takahashi, Anomalous anisotropic magnetoresistance in pseudo-single-crystal γ'-Fe_4N films, Appl. Phys. Express **3**, 113003 (2010).

[26] S. Isogami, K. Takanashi, and M. Mizuguchi, Dependence of anomalous Nernst effect on crystal orientation in highly ordered γ'-Fe_4N films with anti-perovskite structure, Appl. Phys. Express **10**, 073005 (2017).

[27] K. Ito, J. Wang, Y. Shimada, H. Sharma, M. Mizuguchi, and K. Takanashi, Enhancement of the anomalous Nernst effect in epitaxial Fe_4N films grown on $SrTiO_3$(001) substrates with oxygen deficient layers, J. Appl. Phys. **132**, 133904 (2022).

[28] K. Kabara, M. Tsunoda, and S. Kokado, Anomalous Hall effects in pseudo-single-crystal γ'-Fe_4N thin films, AIP Adv. **6**, 055801 (2016).

[29] A. Damascelli, Z. Hussain, and Z.-X. Shen, Angle-resolved photoemission studies of the cuprate superconductors, Rev. Mod. Phys. **75**, 473 (2003).

[30] K. Kabara, M. Tsunoda, and S. Kokado, Annealing effects on nitrogen site ordering and anisotropic magnetoresistance in pseudo-single-crystal γ'-Fe_4N films, Appl. Phys. Express **7**, 063003 (2014).

[31] T. Okuda, K. Miyamaoto, H. Miyahara, K. Kuroda, A. Kimura, H. Namatame, and M. Taniguchi, Efficient spin resolved spectroscopy observation machine at Hiroshima Synchrotron Radiation Center, Rev. Sci. Instrum. **82**, 103302 (2011).

[32] T. Okuda, K. Miyamoto, A. Kimura, H. Namatame, and M. Taniguchi, A double VLEED spin detector for high-resolution three dimensional spin vectorial analysis of anisotropic Rashba spin splitting, J. Electron Spectrosc. Relat. Phenom. **201**, 23 (2015).

[33] T. Okuda and A. Kimura, Spin- and angle-resolved photoemission of strongly spin–orbit coupled systems, J. Phys. Soc. Jpn. **82**, 021002 (2013).

[34] See Supplemental Material at https://link.aps.org/supplemental/10.1103/mlcy-gszb for details of the experimental procedures, surface characterization (LEED and Auger electron spectroscopy (AES)), computational methods, and additional orbital-resolved band structure analysis, which includes Refs. [31,32,S1–S4].

[35] S. Isogami, K. Masuda, Y. Miura, N. Rajamanickam, and Y. Sakuraba, Anomalous Hall and Nernst effects in ferrimagnetic Mn_4N films: Possible interpretations and prospects for enhancement, Appl. Phys. Lett. **118**, 092407 (2021).

[36] S. Isogami, M. Tsunoda, M. Oogane, A. Sakuma, and M. Takahashi, Dependence of magnetic damping on temperature and crystal orientation in epitaxial Fe_4N thin films, J. Magn. Soc. Jpn. **38**, 162 (2014).

[37] M. Fanciulli, J. Schusser, M.-I. Lee, Z. E. Youbi, O. Heckmann, M. C. Richter, C. Cacho, C. Spezzani, D. Bresteau, J.-F. Hergott, P. D'Oliveira, O. Tcherbakoff, T. Ruchon, J. Minár, and K. Hricovini, Spin, time, and angle resolved photoemission spectroscopy on WTe_2, Phys. Rev. Res. **2**, 013261 (2020).

[38] M. Schmitt, O. Kirilmaz, S. Chernov, S. Babenkov, D. Vasilyev, O. Fedchenko, K. Medjanik, Y. Matveyev, A. Gloskovskii, C. Schlueter, A. Winkelmann, L. Dudy, H.-J. Elmers, G. Schönhense, M. Sing, and R. Claessen, Bulk spin polarization of magnetite from spin-resolved hard x-ray photoelectron spectroscopy, Phys. Rev. B **104**, 045129 (2021).

[39] Y. Wan, L. Wang, K. Kuroda, P. Zhang, K. Koshiishi, M. Suzuki, J. Kim, R. Noguchi, C. Bareille, K. Yaji, A. Harasawa, S. Shin, S.-W. Cheong, A. Fujimori, and T. Kondo, Selective observation of surface and bulk bands in polar WTe_2 by laser-based spin- and angle-resolved photoemission spectroscopy, Phys. Rev. B **105**, 085421 (2022).

[40] Y. Fukushima, K. Kawaguchi, K. Kuroda, M. Ochi, M. Hirayama, R. Mori, H. Tanaka, A. Harasawa, T. Iimori, Z. Zhao, S. Tani, K. Yaji, S. Shin, F. Komori, Y. Kobayashi, and T. Kondo, Spin-polarized saddle points in the topological surface states of elemental bismuth revealed by pump-probe spin- and angle-resolved photoemission spectroscopy, Phys. Rev. B **110**, L041401 (2024).

[41] K. Miyamoto, K. Iori, K. Sakamoto, H. Narita, A. Kimura, M. Taniguchi, S. Qiao, K. Hasegawa, K. Shimada, H. Namatame, and S. Blügel, Spin polarized *d* surface resonance state of fcc Co/Cu(001), New J. Phys. **10**, 125032 (2008).

[42] S. Hüfner, *Photoelectron Spectroscopy: Principles and Applications*, 3rd ed. (Springer, Berlin, 2003).

[43] J. J. Yeh and I. Lindau, Atomic subshell photoionization cross sections and asymmetry parameters: $1 \leqslant Z \leqslant 103$, At. Data Nucl. Data Tables **32**, 1 (1985).

[44] T. Valet and A. Fert, Theory of the perpendicular magnetoresistance in magnetic multilayers, Phys. Rev. B **48**, 7099 (1993).

[45] S. Kokado, M. Tsunoda, K. Harigaya, and A. Sakuma, Anisotropic magnetoresistance effects in Fe, Co, Ni, Fe_4N, and half-metallic ferromagnet: A systematic analysis, J. Phys. Soc. Jpn. **81**, 024705 (2012).